

# DISCOVERY OF ROTATIONAL MODULATIONS IN THE PLANETARY-MASS COMPANION 2M1207b: AN INTERMEDIATE ROTATION PERIOD AND HETEROGENEOUS CLOUDS IN A LOW GRAVITY ATMOSPHERE

YIFAN ZHOU<sup>1</sup>, DÁNIEL APAI<sup>1,2,3</sup>, GLENN H SCHNEIDER<sup>1</sup>, MARK S. MARLEY<sup>4</sup>, ADAM P. SHOWMAN<sup>2</sup>

*Draft version November 1, 2015*

## ABSTRACT

Rotational modulations of brown dwarfs have recently provided powerful constraints on the properties of ultra-cool atmospheres, including longitudinal and vertical cloud structures and cloud evolution. Furthermore, periodic light curves directly probe the rotational periods of ultra-cool objects. We present here, for the first time, time-resolved high-precision photometric measurements of a planetary-mass companion, 2M1207b. We observed the binary system with HST/WFC3 in two bands and with two spacecraft roll angles. Using point spread function-based photometry, we reach a nearly photon-noise limited accuracy for both the primary and the secondary. While the primary is consistent with a flat light curve, the secondary shows modulations that are clearly detected in the combined light curve as well as in different subsets of the data. The amplitudes are 1.45% in the F125W and 0.92% in the F160W filters, respectively. We find a consistent period of  $10.5^{+1.5}_{-0.8}$  hours and similar phases in both bands. The J- and H-band amplitude ratio of 2M1207b is very similar to a field brown dwarf that has identical spectral type but different J-H color. Importantly, our study also measures, for the first time, the rotation period for a directly imaged planetary-mass companion to another star.

*Subject headings:* brown dwarfs – planets and satellites: atmospheres – planets and satellites: individual (2M1207b) – techniques: photometric

## 1. INTRODUCTION

Presence of condensate clouds is one the most unique features of the ultra-cool atmosphere of directly imaged exoplanet and brown dwarfs. Studies of formation and properties of condensate clouds (e.g. Ackerman & Marley 2001; Burrows et al. 2006; Helling et al. 2008; Allard et al. 2012) have made great progress on the cloud behaviors across different spectral types, especially the role that clouds play in the L-T transition (e.g. Burrows et al. 2006; Marley et al. 2010). Surface gravity is suggested to be the second key parameters in defining cloud structures (e.g. Marley et al. 2012) after effective temperature. Low surface gravity objects (e.g. HR8799 bcd, Marois et al. (2008), 2M1207b, Chauvin et al. (2004)) are significantly redder and under-luminous compared to field brown dwarfs. The anomalous color and luminosity of low surface gravity objects support models including unusually thick clouds (Currie et al. 2011; Madhusudhan et al. 2011; Skemer et al. 2011, 2012). However, due to lack of observational constraint, the dependence of cloud properties on surface gravity is not very well modeled.

Intensity modulations introduced by heterogeneous clouds can be directly observed and studied via time resolved observation and rotational mapping (e.g. Apai et al. 2013; Buenzli et al. 2012, 2015; Burgasser et al. 2013; Radigan et al. 2012; Yang et al. 2015; Metchev et al.

2015; Heinze et al. 2015; Biller et al. 2015). These techniques isolate the effect of cloud properties and obtained great success in determining the rotation period and unveiling the structures of the atmosphere of brown dwarfs. Kostov & Apai (2013) demonstrated that these techniques can be applied to directly imaged exoplanets, too, allowing comparative studies of objects with different surface gravities. However, high contrast magnifies the challenges for directly imaged exoplanets and planetary-mass companions to acquire high-precision light curves comparing to *isolated* brown dwarfs.

2M1207b Chauvin et al. (2004) is the first directly imaged extra-solar planetary-mass companion. Chauvin et al. (2005) and Song et al. (2006) confirmed that 2M1207b and its host 2M1207A form a bound, co-moving system. 2M1207A and b have an angular separation of 0.78", which corresponds to a projected separation of 41.2 AU at a distance of 52.4 pc (e.g. Ducourant et al. 2008). Combining 2M1207b's age and near infrared luminosity with brown dwarf cooling models (e.g. Baraffe et al. 2003), the object's mass is estimated to be 2.3-4.8 M<sub>Jup</sub> (Barman et al. 2011). Even though a circum-substellar disk was discovered around 2M1207A (Sterzik et al. 2004), the high companion-to-host mass ratio and large separation argue for binary-like gravitational fragmentation formation (Lodato et al. 2005; Mohanty et al. 2007).

Early observations revealed that 2M1207b's color is much redder and its near-infrared luminosity is much lower than those of field brown dwarfs with similar spectra (e.g. Mohanty et al. 2007; Skemer et al. 2011; Barman et al. 2011). 2M1207b's luminosity – as derived from near-infrared photometry – is  $\sim 2.5$  mag lower than that predicted based on its mid- to late L spectral type and effective temperature of  $\sim 1600$  K (Patience et al. 2010).

<sup>1</sup> Department of Astronomy/Steward Observatory, The University of Arizona, 933 N. Cherry Ave., Tucson, AZ, 85721, USA, yifzhou@email.arizona.edu

<sup>2</sup> Department of Planetary Science/Lunar and Planetary Laboratory, The University of Arizona, 1640 E. University Blvd., Tucson, AZ 85718, USA

<sup>3</sup> Earths in Other Solar Systems Team, NASA Nexus for Exoplanet System Science

<sup>4</sup> NASA Ames Research Center, Naval Air Station, Moffett Field, Mountain View, CA 94035, USA

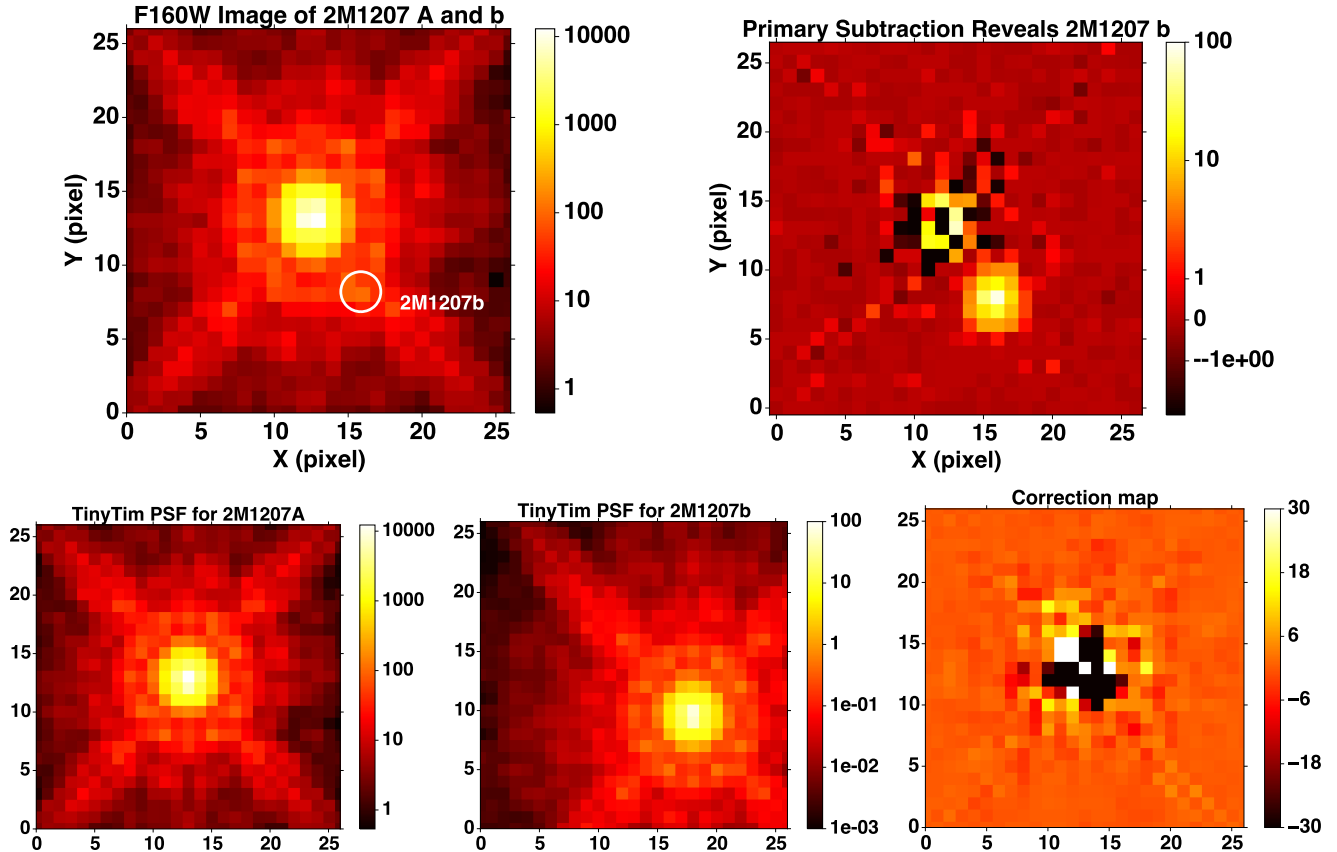


FIG. 1.— Point spread function subtraction allows isolating the secondary and accurately measuring its brightness in our WFC3 F160W images. *Upper row:* original (left) and primary subtracted (right) images. After subtraction of the primary PSF and correction map, 2M1207b is detected at a high significance level. *Lower row: examples of Tiny Tim PSFs for the primary and the secondary, and the correction map.*

Based on multi-band, near-infrared photometry, Skemer et al. (2011) argued that the apparent under-luminosity of 2M1207 b could be explained by a model of a spatially heterogeneous atmosphere composed of patches of thin and patches of unusually thick clouds. Similarly, Barman et al. (2011) argued that non-local chemical equilibrium could play an equally important role as thick clouds in defining 2M1207b’s color and luminosity.

The discovery of additional planetary-mass companions with similarly red colors (*e.g.* AB pic B, Chauvin et al. (2005), HR8799bcde, Marois et al. (2008, 2010)) and apparent under-luminosity have highlighted 2M1207b as a template of low gravity ultra-cool atmospheres but as of now understanding the composition and structure of clouds and their gravity-dependence remained elusive.

In this *Paper* we present the first, high-contrast, high-cadence, high-precision, time-resolved *Hubble Space Telescope* (HST) photometric time series of 2M1207b, a directly imaged planetary-mass object. We successfully detect rotational modulation and measure the amplitudes in two bands and determine the rotational period. These observations probe the spatial heterogeneity and vertical structure of clouds in planetary mass objects for the first time.

## 2. OBSERVATION

We obtained direct images of the 2M1207A+b system on UT 2014 April 11 from 08:07:47 (*JD* 2456758.838738) to 16:53:18 *JD* 2456759.203681 using HST and its Wide Field Camera 3 (WFC3, pixel scale=0.130mas/pixel, MacKenty et al. 2008) in the frame of the HST Program GO-13418 (PI: D. Apai). We acquired the observations in filters F125W ( $\lambda_{\text{pivot}} = 1245.9$  nm, full width at half maximum (FWHM) = 301.5 nm) and F160W ( $\lambda_{\text{pivot}} = 1540.52$ , FWHM = 287.9 nm), roughly corresponding to the J and H bands. We used the  $256 \times 256$  pixels sub-array mode to avoid memory dumps during the observations. In order to provide a near-continuous coverage for detecting modulations we observed the 2M1207 system in 6 consecutive HST orbits, obtaining data with *maximum* cadence of 1.78 minutes over a baseline of 8 hours and 40 minutes. The observations were interrupted by 58-minute long Earth occultations every 94 minutes.

The observations applied space craft rolls each two orbits to allow roll-subtraction of the primary (*e.g.* Song et al. 2006). The telescope roll angles for orbit 1, 3, and 5, and those for 2, 4, and 6 differed by  $25^\circ$ . At the separation of 2M1207b, this angle difference corresponds to a displacement of  $0.34''$ , or 2.75 and 2.30 resolution elements in F125W and F160W, respectively. *In each orbit, we took 8 SPARS 10 exposure sequences alternating between F125W and F160W filters. Each sequence contained 2–3 identical exposures*

*that had 10 non-destructive read-outs and total exposure time of 88.4 s* To improve sampling and reduce the risk that the core of point spread function (PSF) is affected by bad pixels, we applied a 4-point dither pattern with differential “X/Y” offsets of 1.375” in the detector frame, providing optimal non-integral (half pixel) step of 10.5 and 8.5 pixels in F125W and F160W, respectively. In total, we obtained 70 and 64 images with 10 in F125W and F160W, respectively.

### 3. DATA REDUCTION

#### 3.1. Photometry

We started the reduction from the `flt` files produced by the WFC3’s `calwfc3` pipeline. We did not opt to use `ima` files that contain all non-destructive read-outs, because they provided less information on 2M1207A, which saturated after the first few samples. The `flt` files are results of basic calibration, including dark current correction, non-linearity correction, flat field correction, as well as up-the-ramp fit on the non-destructive read-outs. Pixels with data quality flags “bad detector pixels”, “unstable response”, and “bad or uncertain flat value” were masked out and excluded from further analysis as suggested by previous transit exoplanet spectroscopic observations (e.g. Berta et al. 2012; Kreidberg et al. 2014).

The major challenge of high contrast observation with WFC3/IR is the fact that the detector is significantly under-sampled. 2M1207A and b are only separated by  $\sim 6$  pixels or  $\sim 5$  FWHM of the PSF on the detector. When applying roll subtraction, notable artifacts are introduced by image shifting and interpolation. *Tiny Tim* PSF simulator (Krist 1995) offers a solution by providing Nyquist or better sampled PSF, but systematic errors of *Tiny Tim* PSF for WFC3 limits its ability in high precision photometry (Biretta 2014). Building on the large number of PSFs obtained in our program at two different roll angles, we followed a novel, two-step approach that uses a hybrid PSF. First, based on our observations, we derived correction maps for *Tiny Tim* that accurately described the scattered light component for the primary at the correct location on the detector. Second, we carried out a PSF-photometry using hybrid PSFs composed by *Tiny Tim* PSFs and the correction map by simultaneously minimizing the residuals from the primary and the secondary.

For both of 2 steps, we used *Tiny Tim* to calculate  $10\times$  over-sampled model PSFs based on the filters, the spectra (2M1207A: Bonnefoy et al. (2014), 2M1207b: Patience et al. (2010)), the telescope’s actual focus, and the telescope jitter. We used the set of *Tiny Tim* parameters provided by Biretta (2014) to improve modeling the cold mask, diffraction spikes, and the coma. The focus parameters are interpolated to the precise time of the observations using the tabulated values provided by STScI<sup>5</sup>. To align the *Tiny Tim* PSF to the observed PSF of 2M1207A, we moved the over-sampled PSF on a coordinate grid (grid size=0.001 pixel) using cubic interpolation, and searched for the position that minimizes the rms difference of the observed and the re-binned *Tiny Tim* PSF over a region centered on 2M1207A with a 5-pixel-radius aperture centered on 2M1207b excluded.

Then we introduced another *Tiny Tim* PSF for 2M1207b and fit the position of 2M1207b and the scales of the *Tiny Tim* PSFs of 2M1207A and b simultaneously by minimizing the residual from both primary and secondary. In the first step, we discovered that the difference of observed PSFs and model PSFs was very stable for a specified telescope roll angle and dithering position. Therefore, at the end of the first step, we derive 8 (2 roll angles  $\times$  4 dithering positions) correction maps for each filter:

$$\text{Corr} = \text{Median}(\text{PSF}_{\text{obs.}} - \text{PSF}_{\text{model}}) \quad (1)$$

where  $\text{PSF}_{\text{model}}$  was a combination of two scaled *Tiny Tim* PSFs for 2M1207A and b. In the second round, we combined the correction map linearly with the two *Tiny Tim* PSFs to generate hybrid PSFs, and scaled the correction map together with the two PSFs so that the residual, which is expressed as

$$\text{residual} = \text{Image} - a \cdot \text{PSF}_A - b \cdot \text{PSF}_b - c \cdot \text{Corr} \quad (2)$$

is minimized by least square fitting. We found that by introducing the correction term, the reduced  $\chi^2$  was decreased from  $\sim 10$  to  $\sim 1$ . Relative photometry was acquired from the scaling parameters of the *Tiny Tim* PSFs.

Our final step was to correct for a slight apparent trend between the position of the targets on the detector and their flux. We attributed this to a combination of slight changes in the PSF profile due to pixelation and to the effect of imperfectly corrected pixel-to-pixel sensitivity variations. We corrected for these apparent position-dependent flux changes by normalizing each photometric point by the median of all fluxes measured when the target was at the same position, i.e. combining data over 6 orbits. We note that this correction was small and, as we demonstrate in the next sections, could not introduce artificial modulations that resemble the long-period variations that we identified in 2M1207b.

As our study is the first to present high-contrast, high-cadence observations, we provide a detailed analysis of the uncertainties and their impact on our results.

#### 3.2. Uncertainty Analysis: White noise

First we estimated the photon noise for the photometry of 2M1207b. The total photon noise of the photometry was calculated by combining the photon noise of every pixel, which was derived from count rates and detector gain. The photon noises in F125W and F160W are 1.33% and 1.02%, respectively.

Since the PSFs for the 2M1207A and b were fitted simultaneously, the uncertainties for photometry and position of the primary and secondary were coupled. Errors in position measurements of 2M1207A could potentially affect the photometry of 2M1207b. We used a Monte Carlo (MC) method to evaluate the overall systematics of the PSF fitting. We applied photometry to images that were added with random Poisson noise and repeated the photometry procedure for 1000 times. The uncertainties for F125W and F160W photometry were found to be 1.34% and 1.12%, respectively.

#### 3.3. Uncertainty Analysis: Flat field uncertainties

A further contribution to photometric uncertainties may be introduced by imperfectly corrected pixel-to-pixel sensitivity differences. 2M1207b were observed at 8

<sup>5</sup> <http://www.stsci.edu/hst/observatory/focus/FocusModel>

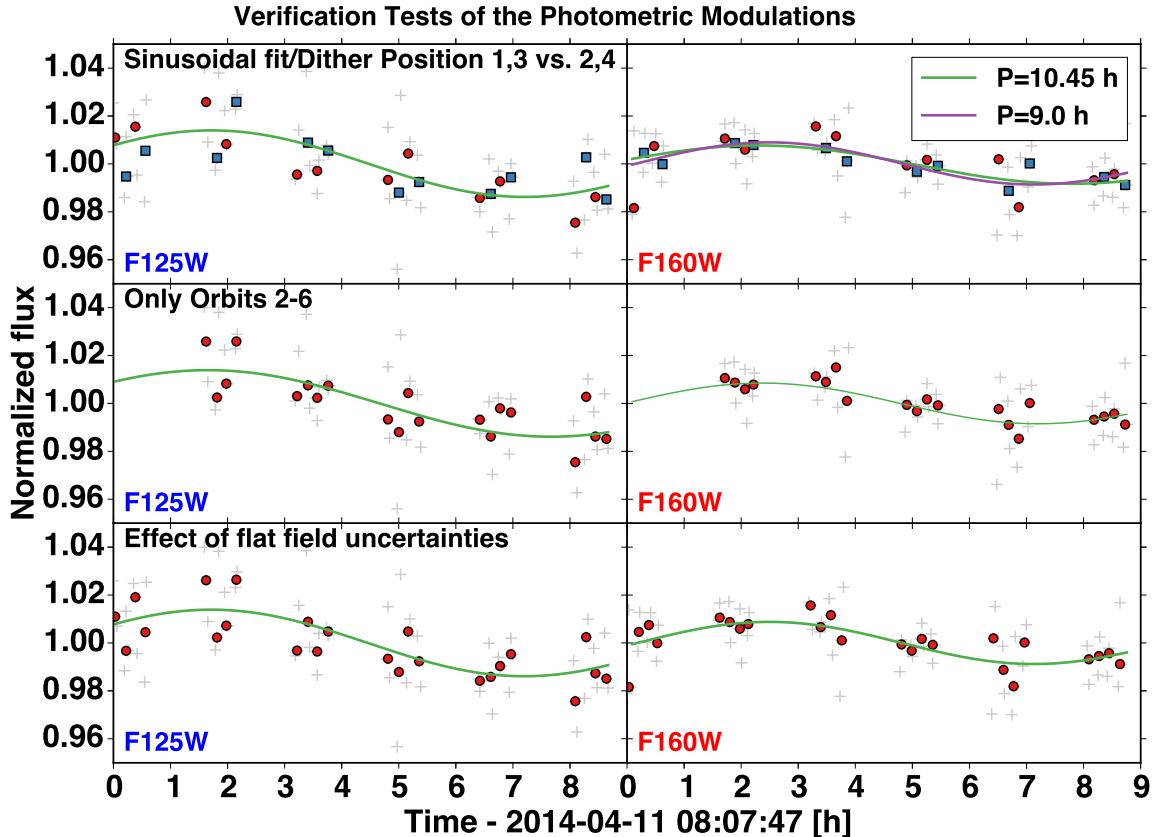


FIG. 2.— F125W (left) and F160W (right) light curves under different variability verification tests. Individual measurements are plotted with gray crosses. Photometric measurements of the same exposure sequence are binned, and binned photometry are plotted with points or squares. Best fitted sinusoids are plotted with solid lines. *Upper*: binned measurements taken in dithering position 1 and 3 (red points) and that taken in 2 and 4 (blue squares) are plotted with different symbols. They demonstrate same trend of modulation. In upper left panel, the green line a sinusoid fitted with all parameters freely varying, and the purple line is a sinusoid fitted with the period set the same as that of F125W. *Middle*: sinusoids fitted without using the data taken in Orbit #1. These curves are almost identical to the curves plotted in upper panel. *Lower*: photometry measured with AFEM-added images and best fitted sinusoids. These points and curves are also almost identical to those plotted in the upper panel.

different positions on the detector (2 rolls  $\times$  4 dithering positions). Imperfect flat field correction could introduce position-dependent differences in the count rates. The uncertainty of WFC3 IR flat field is typically  $\sim 1\%$  (Dressel 2012).

In PSF photometry, however, multiple pixels are fitted simultaneously, so that we expect the photometry to be less affected by high spatial frequency flat field noise, and have a lower than 1% uncertainty from the flat field errors. To verify this, we multiplied every image by an artificial flat field error mask (AFEM) – a uniformly distributed Gaussian noise array with mean of 1 and sigma of 1% – and repeated the PSF photometry on the resulting images. The analysis of these experiments resulted in almost identical light curve to the original, verifying that the flat field errors did not affect our photometry significantly (Figure 2, bottom panel).

#### 4. VERIFICATION OF PHOTOMETRIC MODULATIONS AND AMPLITUDE ESTIMATE

##### 4.1. Tests and Verification

The light curves that resulted from our photometry showed apparently sinusoidal modulations, discussed in more detail in §3.3. To verify that these modulations are intrinsic to the object and not the result of our data

reduction procedures or instrumental changes, we carried out three different tests.

First, we fitted sinusoids independently to the light curves of two filters to verify the similarity of the signal in the two bands (Figure 2, top panel). Inconsistent periods or light curve shapes would argue against a genuine signal. We found that the periods of the best fit sine waves were similar,  $10.5^{+1.2}_{-1.3}$  h for F125W and  $9.1^{+1.1}_{-1.0}$  h for F160W. These periods are consistent within the uncertainty. Furthermore, these periods are not close to any timescales over which HST or WFC3 changes, and are very different from all timescales present in our observations (dithering timescales, integration times, and orbital timescales).

As a second test, we repeated the analysis neglecting the first orbit. The motivation behind this test is that, due to spacecraft thermal settling, the first orbits of HST observations are often slightly unstable, and are neglected in high-precision studies (e.g. Mandell et al. 2013). Indeed, in our analysis, 2M1207A is significantly fainter in the first orbit (Figure 3) than in the subsequent ones. Our analysis based on orbits 2–6 found essentially identical results to our analysis using the whole 6 orbits, based on which we conclude that the first less reliable orbit does not affect our results significantly (Figure 2,



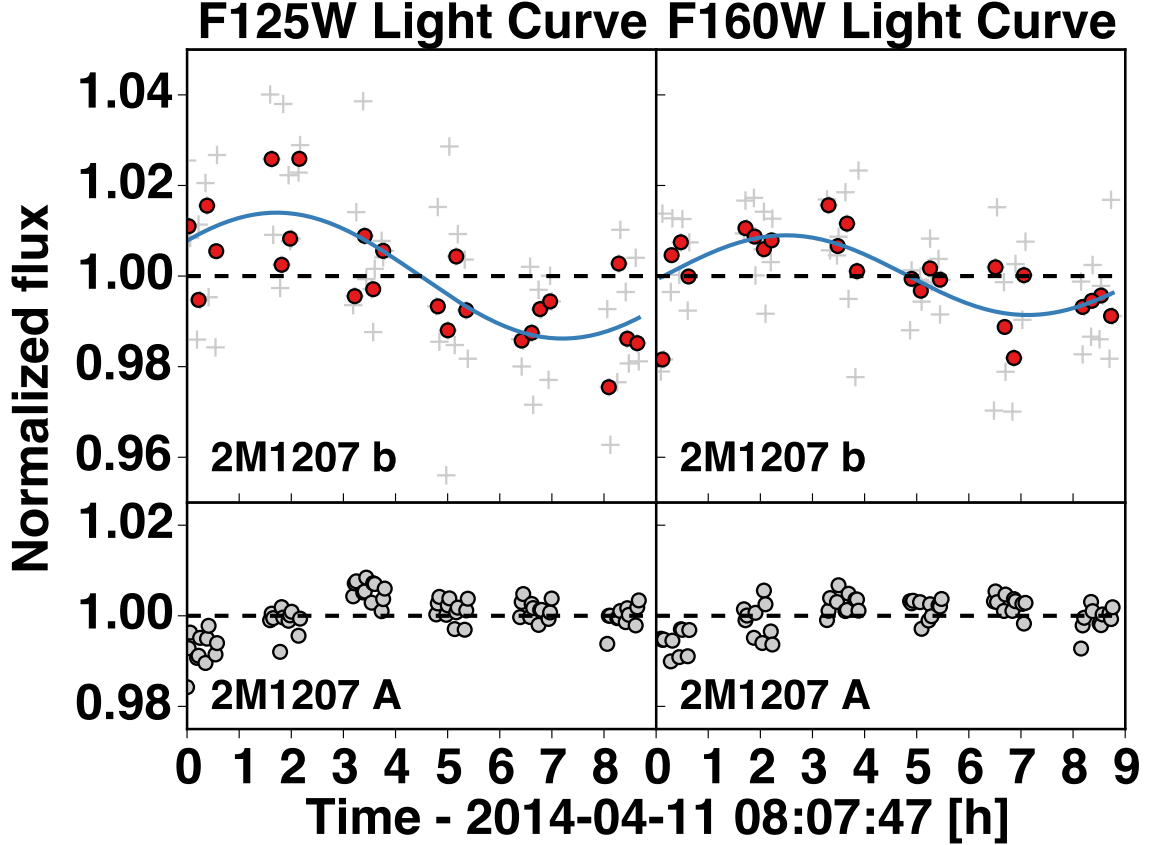


FIG. 3.— Normalized light curves for 2M1207 B (upper) and A (lower) with filter F125W (left) and F160W (right). Unbinned measurements are plotted in gray crosses and binned photometry are plotted with red points. Best fitted sinusoids are plotted with blue solid lines.

middle panel).

As a third test, we explored whether a subset of images, perhaps due to imperfect normalization or correlation with specific instrument states, could drive the light curves into apparently sinusoidal shapes. To test this possibility, we split the data into two temporally overlapping halves: subset one were images taken at dithering position 1 and 3; subset two were those taken at dithering position 2 and 4. For both subsets, we repeated our analysis independently. For both of F125W and F160W, two halves demonstrated similar sinusoidal modulations. Our analysis detect sinusoidal modulations in *both* subsets and in *both* filters, with periods and amplitudes consistent with those derived from the complete data set (Figure 2, upper panel).

These tests demonstrate that the modulation seen in our data are consistently present in the different filters, in the different time segments of the data, and in data obtained in different dithering positions. All of the three tests support the signal to be intrinsic to the target.

#### 4.2. Amplitude and Period Measurements

*To further constrain the amplitude and period of the light curve, we performed sinusoidal fit using Markov Chain Monte Carlo (MCMC) method. The priors for the amplitude, the period and the phase of the sinusoid were all assumed to be uniform distributions. The ranges of the prior distributions were 0 to 5% for the ampli-*

*tude, 2 to 40 hours for the period, and 0 to  $2\pi$  for the phase. The posterior distributions of the period and amplitude were very well constraint for both two filters so that we were able to measure the amplitudes and periods as well as their uncertainties. We also did the fitting excluding data from the first orbit. In this case, posterior distributions are not as well constraint as those for including all the data, especially the posterior distributions for period have significant proportion at the long period end. However, for both two filters, the positions of the peaks of distributions of period and amplitude agree within  $1-\sigma$  uncertainty with or without including data from the first orbit.*

*We note that if the data from the first orbit were excluded, the light curves could be reasonably fitted to a linear trend. When ignoring data from the first orbit, For F125W light curve, the reduced  $\chi^2$  for sinusoidal and linear fits are 1.138 and 1.143, and for F160W are 0.944 and 0.953. However, We are in favor of the sinusoidal model based on physical viability (See detailed discussion in §6).*

## 5. RESULT

We present the first high-contrast, high-cadence, and high-precision photometry of a directly imaged planet or planetary-mass companion around another star. Our

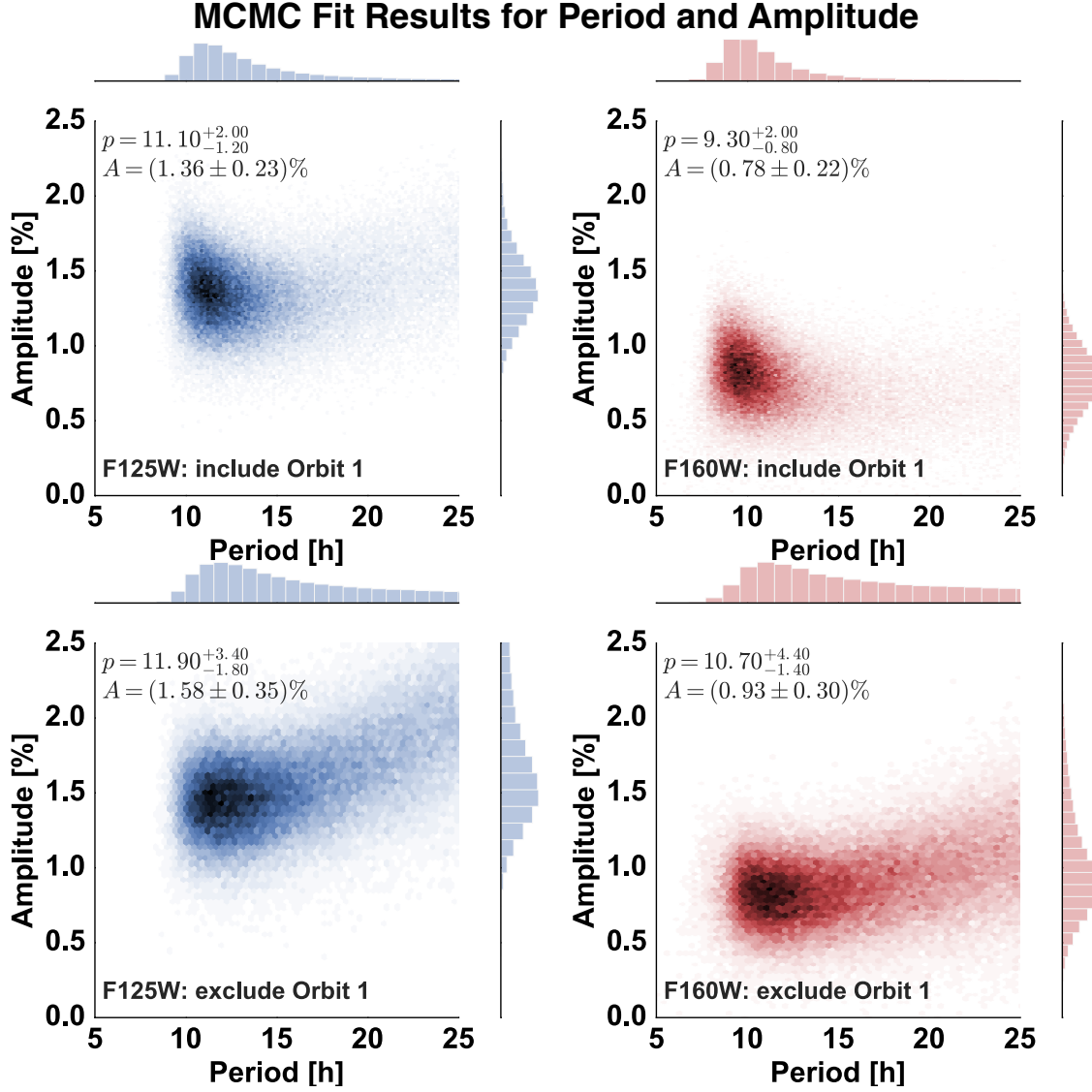


FIG. 4.— *Posterior distribution for amplitude and period for F125W (left) and F160W (right) light curves, with the data from the first orbit included (upper) and excluded (lower). In each panel, the univariate distributions for period and amplitude are plotted along side with the joint distributions. The measurements and uncertainties of period and amplitude are shown on the upper left corner of each panel.*

observations reveal a modulation in the light curve of the  $\sim 4M_{\text{Jup}}$  companion 2M1207b, the first detection of modulations in directly imaged planetary-mass objects. The best fit periods for F125W and F160W are  $11.1^{+2.0}_{-1.2}$  and  $9.3^{+2.0}_{-0.8}$  hours, respectively. We also fitted the two band light curves together forcing the periods of two sinusoids to be the same, and obtained a period of  $10.5^{+1.5}_{-0.8}$  hours.

We obtained high signal to noise photometry for both 2M1207A and B (Figure 3). On average, the photometric contrast is  $6.52 \pm 0.01$  mag for F125W and  $5.77 \pm 0.01$  mag for F160W.

We find that the amplitudes in the two bands are significantly different. By fitting Gaussians to the MC fit result distributions, we determine that the amplitude for F125W is 1.45% with a standard deviation of 0.22%, and the amplitude for F160W is 0.92% with a standard de-

viation of 0.20%. The amplitudes of two bands are separated by more than  $2\text{-}\sigma$ . The amplitude for F125W is  $1.58 \pm 0.27$  times of that for F160W light curve.

## 6. DISCUSSION

An important result of our study is the direct measurement of the photometric modulation period of a directly imaged planetary-mass object. *Although a linear trend can also provide reasonable fit to the light curves when data from the first orbit are excluded, it is not a physical viable model. The light curve of a planetary mass companion is either a complete flat line, or a periodical curve with constant mean. On the contrary, 2M1207b is not likely to constantly getting bright or faint. The flatness of the light curves of 2M1207A demonstrate that there is no instrumental sensitivity drift or any similar effect that can introduce a*

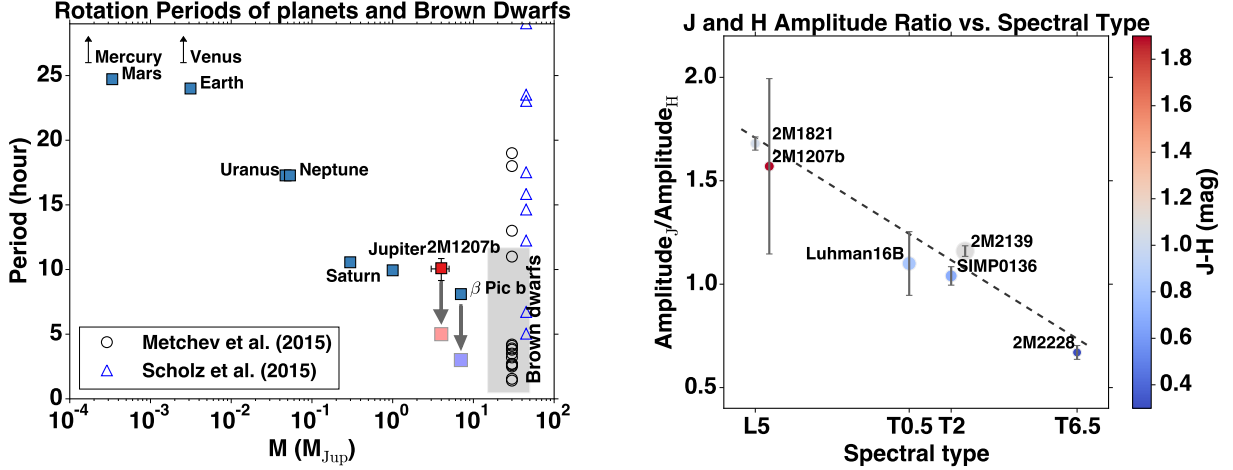


FIG. 5.— comparison of 2M1207b’s rotation period and color change with brown dwarfs,  $\beta$  Pic b, and solar system planets. *Left*: period vs. mass plot for 2M1207b (red square), solar system planets and  $\beta$  Pic b (blue squares), field brown dwarfs from the study of Metchev et al. (2015) (black circles, gray shade) and young brown dwarfs from the study of Scholz et al. (2015) (blue triangles). Final rotation rates for 2M1207b and  $\beta$  Pic b estimated based on conservation of angular momentum are plotted with faint red and blue squares, respectively. The mass of brown dwarfs are assumed to be  $\sim 30 M_{\text{Jup}}$ , and the difference mass of field brown dwarfs and young brown dwarfs are added artificially for the sake of clarity. The gray rectangle that has a  $\pm 15 M_{\text{Jup}}$  range in  $x$ , and a  $\pm \sigma$  of field brown dwarf periods range in  $y$ , indicates a region where field brown dwarfs most likely to appear in this diagram. Rotation period monotonically decreases with the increase of mass. *Right*: ratio of modulation amplitude in J and H band vs. spectral type for 2M1207b and brown dwarfs. The point for 2M1207b is shifted to  $+x$  for half spectral type for clarification. The colors of the points represent J–H magnitude, and the sizes of the points are proportional to the J-band modulation amplitudes. The gray dashed line is the result of a linear fit to these points. Correlation of J- and H-band modulation amplitude ratio and spectral type is shown.

*$\sim 9$  hour slope. We do include very long period sinusoid as possible solution for our MC fit, and demonstrate that a sinusoid with period of  $\sim 10$  hour is the most probable solution with or without including data from the first orbit.* We infer the rotation period of 2M1207b to be the same as the period of photometric variation. Although horizontal winds can cause the measured period to differ from true rotation period, it is unlikely that the difference is greater than the uncertainty of the measurement, since for Jupiter and Saturn, typical wind speeds are more than one order of magnitude smaller than the equatorial rotation speeds. In the left panel of Figure 5 we compare the rotation period of 2M1207b to the solar system planets,  $\beta$  Pic b the only other directly imaged planet with an estimated period and measured  $v \sin i$ , field brown dwarfs from the study of (Metchev et al. 2015), and young brown dwarfs (UpSco, age  $\sim 11$  Myr) from (Scholz et al. 2015). Snellen et al. (2014) measured  $v \sin i$  for  $\beta$  Pic b and demonstrated that it fits a trend defined by Solar System planets in which more massive planets have faster rotation rates. The interesting finding that  $\beta$  Pic b, an exoplanet that formed in a protoplanetary disk, follows this trend suggests a possibly connection between planet mass, initial angular momentum, and formation in a disk.

Excitingly, our measurement of the rotation period of 2M1207b, a planet mass companion that has similar age to  $\beta$  Pic b, has a rotation period that fits in the same trend, as well as majority of the brown dwarfs. As 2M1207b and  $\beta$  Pic b evolve and cool down, they are expected to shrink to the size of Jupiter. Order of magnitude estimation based on the conservation of angular momentum results in final rotation periods of  $\sim 5$  h and  $\sim 3$  hours (Snellen et al. 2014) for 2M1207b and  $\beta$  Pic b, respectively, which still fit to the period vs. mass trend.

Although 2M1207A is known to host a circumsubstellar disk (Sterzik et al. 2004), the low mass of typical brown dwarf disks (Klein et al. 2003; Mohanty et al. 2013, e.g.) and its large separation argue against the possibility that 2M1207b has formed in a protoplanetary disk. The result that objects formed in different scenarios share the same trend of period vs. mass suggests that rotation periods – in absence of well-determined ages – may contribute insufficient evidence for a formation in a disk vs. in a cloud core environment.

*Rotation period of  $\sim 10$  hour is significantly larger than field brown dwarfs from the sample of Metchev et al. (2015), but comparable to the median period of the sample of Scholz et al. (2015), of which the age is similar to 2M1207b. The rotation period of 2M1207b is agreed within the range predicted by evolutionary track established from measurements of brown dwarfs assuming conservation of angular momentum (Fig. 4 in Scholz et al. (2015)), and much longer than the break-up limit, i.e. the rotation period where the equatorial centrifugal force exceeded gravitational force. Observed rotation rate for brown dwarfs of different ages show little evidence of angular momentum loss at the age of several Myr as oppose to low mass stars (Bouvier et al. 2014; Scholz et al. 2015), and agree with the model of solid body rotation for the fully convective interior. Rotation periods of planetary mass objects with well established age measurement, can place stronger constrain on the internal structure, since angular momentum loss through disks is even less likely comparing with brown dwarfs.*

Our inferred rotation period is very similar to those of Jupiter and Saturn, which have periods of 9.9 and 10.5 hours, respectively. Moreover, our inferred rotation

is sufficiently fast that – just as with Jupiter and Saturn – the atmospheric dynamics is likely to be rotationally dominated at regional to global scales (Showman & Kaspi 2013). The importance of rotation can be characterized by the Rossby number  $Ro = U/\Omega L$ , where  $U$  is the characteristic wind speed,  $\Omega$  is the angular rotation rate ( $1.7 \times 10^{-4} \text{ s}^{-1}$  for a 10-hour rotation period), and  $L$  is the characteristic horizontal length scale. Showman & Kaspi (2013) presented a theory of the atmospheric circulation on brown dwarfs and directly imaged giant planets, which predicts wind speeds in the range of tens to hundreds of  $\text{ms}^{-1}$  depending on parameters. Using similar arguments, Apai et al. (2013) argued for wind speeds of a few hundreds  $\text{ms}^{-1}$  (somewhat faster than typical in Jupiter) in two L/T transition brown dwarfs. Global simulations of the atmospheric circulation using a one-layer model by Zhang & Showman (2014) predict a similar range. Considering wind speeds ranging from 10 to  $1000 \text{ ms}^{-1}$ , a circulation that is global in scale ( $L=R_{\text{Jup}}$ ) implies Rossby numbers of 0.001 to 0.1 on 2M1207b (see Figure 1 in Showman & Kaspi (2013)). For a circulation whose length scale is  $0.1 R_{\text{Jup}}$ , the Rossby numbers would range from 0.01 to 1 depending on wind speed. Thus, over almost the full range of plausible parameters, we expect that the large-scale circulation on 2M1207b – like Jupiter, Saturn, and most brown dwarfs – exhibits a Rossby number much less than one. This implies that the atmospheric circulation is rotationally dominated and that the horizontal force balance is approximately geostrophic, that is, a balance between Coriolis and pressure-gradient forces.

From the perspective of atmospheric dynamics, 2M1207b exhibits other important similarities to brown dwarfs. Its high effective temperature indicates that – like most brown dwarfs – 2M1207b exhibit a strong interior heat flux presumably transported by convection, and that, by comparison, the external irradiation is negligible to the circulation. These similarities suggest that the overall dynamical mechanisms for driving an atmospheric circulation on 2M1207b should be similar to those on brown dwarfs. Thus, given the prevalence of infrared light curve variability observed on brown dwarfs, it is expected to find such variability on directly imaged planets like 2M1207b. Nevertheless, directly imaged planets generally have lower surface gravity than field brown dwarfs, and this will affect the details of the atmospheric circulation, potentially including the cloud patchiness. Further observations of 2M1207b and other directly imaged planets will help to elucidate these differences. Key questions for the future will include assessing the extent to which the atmospheric circulation on 2M1207b – including the existence of absence of zonal (east-west) jet streams, vortices, storms, and turbulence, and their effect on cloud patchiness – are similar or different than that on typical field brown dwarfs.

Our observations also allow us to compare the relative amplitudes in the J- and H-bands with the handful of brown dwarfs for which high-quality near-infrared time-resolved observations have been obtained. In the right panel of Figure 5, we compare the relative amplitude of J- and H-bands of 2M1207b and brown dwarfs (Apai et al. 2013; Buenzli et al. 2012, 2015; Yang et al. 2015) that have different spectral types and J–H colors. J and H

band fluxes for brown dwarfs are integrated from WFC3 grism spectra using standard J and H filter transmission profile. We find an interesting possible correlation between the spectral types of the objects and their J- to H-band amplitude ratios. In the right panel of Figure 5, we show that earlier spectral type objects have larger amplitudes at shorter wavelength than at longer wavelengths. Interestingly, although the J–H color of 2M1207b is significantly redder, its relative amplitude ratio is very similar to that of 2M1821, which also has an L5 spectral type (Yang et al. 2015). This exciting, but tentative trend must be confirmed with a larger sample of sources that also sample a broader range of surface gravities as well as spectral types. If the larger sample verifies the trend suggested by our small sample, the amplitude ratio will provide a powerful probe of the spectral type and surface gravity dependence of vertical cloud structure.

*Recently, Karalidi et al. (2015) published Aeolus, an atmosphere mapping code that retrieves 2-dimension atmosphere features from the light curves. In the future, with higher signal-to-noise light curves, we will be able to study more detailed structure of the atmospheres of directly imaged exoplanets with this tool.*

## 7. CONCLUSIONS

In summary, from our J- and H-band high precision, high-cadence light curves we discovered sinusoidal modulations in the planetary-mass object 2M1207b. This is the first detection of rotational modulations in a directly imaged planetary-mass object. The period is  $10.2^{+0.9}_{-0.8}$  hours, similar to that derived from  $v \sin i$  measurements for the directly imaged exoplanet  $\beta$  Pic b, significantly longer than most field brown dwarfs with known rotation periods, and *comparable to the brown dwarfs in a sample with similar age to 2M1207b*. The amplitude ratio of J- and H-band is very similar to that of a field brown dwarf with identical L5 spectral type, although they have very different J–H colors.

Finally, we note that the observations presented here open an exciting new window on directly imaged exoplanets and planetary-mass companions. Our study demonstrates a successful application of high contrast, high-cadence, high-precision photometry with planetary mass companion. We also show that these observations can be carried out simultaneously at multiple wavelengths, allowing us to probe multiple pressure levels. With observation of a larger sample and at multiple wavelengths, we will be able to explore the detailed structures of atmospheres of directly imaged exoplanets, and identify the key parameters that determine these.

Support for program number 13418 was provided by NASA through a grant from the Space Telescope Science Institute, which is operated by the Association of Universities for Research in Astronomy, Inc., under NASA contract NAS5-26555. The results reported herein benefited from collaborations and/or information exchange within NASA’s Nexus for Exoplanet System Science (NExSS) research coordination network sponsored by NASA’s Science Mission Directorate. M.S.M. acknowledges support from the NASA Astrophysics Theory Program. A.P.S.



acknowledges support from NSF grant AST1313444.

## REFERENCES

- Ackerman, A. S. & Marley, M. S. 2001, *ApJ*, 556, 872
- Allard, F., Homeier, D., & Freytag, B. 2012, *Royal Society of London Philosophical Transactions Series A*, 370, 2765
- Apai, D., Radigan, J., Buenzli, E., Burrows, A., Reid, I. N., & Jayawardhana, R. 2013, *ApJ*, 768, 121
- Baraffe, I., Chabrier, G., Barman, T. S., Allard, F., & Hauschildt, P. H. 2003, *A&A*, 402, 701
- Barman, T. S., Macintosh, B., Konopacky, Q. M., & Marois, C. 2011, *ApJ*, 735, L39
- Berta, Z. K., Charbonneau, D., Désert, J.-M., et al. 2012, *ApJ*, 747, 35
- Biller, B. A., Vos, J., Bonavita, M., Buenzli, E., Baxter, C., Crossfield, I. J. M., Allers, K., Liu, M. C., Bonnefoy, M., Deacon, N., Brandner, W., Schlieder, J. E., Dupuy, T., Kopytova, T., Manjavacas, E., Allard, F., Homeier, D., & Henning, T. 2015, *ArXiv e-prints*
- Biretta, J. 2014, *Space Telescope WFC Instrument Science Report*, 1, 10
- Bonnefoy, M., Chauvin, G., Lagrange, A.-M., Rojo, P., Allard, F., Pinte, C., Dumas, C., & Homeier, D. 2014, *A&A*, 562, A127
- Bouvier, J., Matt, S. P., Mohanty, S., Scholz, A., Stassun, K. G., & Zanni, C. 2014, *Protostars and Planets VI*, 1, 433
- Buenzli, E., Apai, D., Morley, C. V., Fplateau, D., Showman, A. P., Burrows, A., Marley, M. S., Lewis, N. K., & Reid, I. N. 2012, *ApJ*, 760, L31
- Buenzli, E., Saumon, D., Marley, M. S., Apai, D., Radigan, J., Bedin, L. R., Reid, I. N., & Morley, C. V. 2015, *ApJ*, 798, 127
- Burgasser, A. J., Sheppard, S. S., & Luhman, K. L. 2013, *ApJ*, 772, 129
- Burrows, A., Sudarsky, D., & Hubeny, I. 2006, *ApJ*, 640, 1063
- Chauvin, G., Lagrange, A.-M., Dumas, C., Zuckerman, B., Mouillet, D., Song, I., Beuzit, J.-L., & Lowrance, P. 2004, *A&A*, 425, L29
- . 2005, *A&A*, 438, L25
- Chauvin, G., Lagrange, A.-M., Zuckerman, B., Dumas, C., Mouillet, D., Song, I., Beuzit, J.-L., Lowrance, P., & Bessell, M. S. 2005, *A&A*, 438, L29
- Currie, T., Burrows, A., Itoh, Y., Matsumura, S., Fukagawa, M., Apai, D., Madhusudhan, N., Hinz, P. M., Rodigas, T. J., Kasper, M., Pyo, T.-S., & Ogino, S. 2011, *ApJ*, 729, 128
- Dressel, L. 2012, *Wide Field Camera 3, HST Instrument Handbook*, 1
- Ducourant, C., Teixeira, R., Chauvin, G., Daigne, G., Le Campion, J.-F., Song, I., & Zuckerman, B. 2008, *A&A*, 477, L1
- Heinze, A. N., Metchev, S., & Kelllogg, K. 2015, *ApJ*, 801, 104
- Helling, C., Ackerman, A., Allard, F., Dehn, M., Hauschildt, P., Homeier, D., Lodders, K., Marley, M., Rietmeijer, F., Tsuji, T., & Woitke, P. 2008, *MNRAS*, 391, 1854
- Karalidi, T., Apai, D., Schneider, G., Hanson, J. R., & Pasachoff, J. M. 2015, *ArXiv e-prints*
- Klein, R., Apai, D., Pascucci, I., Henning, T., & Waters, L. B. F. M. 2003, *ApJ*, 593, L57
- Kostov, V. & Apai, D. 2013, *ApJ*, 762, 47
- Kreidberg, L., Bean, J. L., Désert, J.-M., et al. 2014, *Nature*, 505, 69
- Krist, J. 1995, in *Astronomical Data Analysis Software and Systems IV*, Vol. 77, 349
- Lodato, G., Delgado-Donate, E., & Clarke, C. J. 2005, *Mon. Not. R. Astron. Soc. Lett.*, 364, L91
- MacKenty, J. W., Kimble, R. A., O’Connell, R. W., & Townsend, J. A. 2008, in *Society of Photo-Optical Instrumentation Engineers (SPIE) Conference Series*, Vol. 7010, *Society of Photo-Optical Instrumentation Engineers (SPIE) Conference Series*, 1
- Madhusudhan, N., Burrows, A., & Currie, T. 2011, *ApJ*, 737, 34
- Mandell, A. M., Haynes, K., Sinukoff, E., et al. 2013, *ApJ*, 779, 128
- Marley, M. S., Saumon, D., Cushing, M., Ackerman, A. S., Fortney, J. J., & Freedman, R. 2012, *ApJ*, 754, 135
- Marley, M. S., Saumon, D., & Goldblatt, C. 2010, *ApJ*, 723, L117
- Marois, C., Macintosh, B., Barman, T., Zuckerman, B., Song, I., Patience, J., Lafrenière, D., & Doyon, R. 2008, *Science*, 322, 1348
- Marois, C., Zuckerman, B., Konopacky, Q. M., Macintosh, B., & Barman, T. 2010, *Nature*, 468, 1080
- Metchev, S. A., Heinze, A., Apai, D., Fplateau, D., Radigan, J., Burgasser, A., Marley, M. S., Artigau, E., Plavchan, P., & Goldman, B. 2015, *ApJ*, 799, 154
- Mohanty, S., Greaves, J., Mortlock, D., Pascucci, I., Scholz, A., Thompson, M., Apai, D., Lodato, G., & Looper, D. 2013, *ApJ*, 773, 168
- Mohanty, S., Jayawardhana, R., Huelamo, N., & Mamajek, E. 2007, *ApJ*, 657, 1064
- Patience, J., King, R. R., De Rosa, R. J., & Marois, C. 2010, *A&A*, 517, A76
- Radigan, J., Jayawardhana, R., Lafrenière, D., Artigau, E., Marley, M., & Saumon, D. 2012, *ApJ*, 750, 105
- Scholz, A., Kostov, V., Jayawardhana, R., & Mužić, K. 2015, *ApJ*, 809, L29
- Showman, A. P. & Kaspi, Y. 2013, *ApJ*, 776, 85
- Skemer, A. J., Close, L. M., Szűcs, L., Apai, D., Pascucci, I., & Biller, B. A. 2011, *ApJ*, 732, 107
- Skemer, A. J., Hinz, P. M., Esposito, S., Burrows, A., et al. 2012, *ApJ*, 753, 14
- Snellen, I. A. G., Brandl, B. R., de Kok, R. J., Brogi, M., Birkby, J., & Schwarz, H. 2014, *Nature*, 509, 63
- Song, I., Schneider, G., Zuckerman, B., Farihi, J., Becklin, E. E., Bessell, M. S., Lowrance, P., & Macintosh, B. A. 2006, *ApJ*, 652, 724
- Sterzik, M. F., Pascucci, I., Apai, D., van der Blik, N., & Dullemond, C. P. 2004, *A&A*, 427, 245
- Yang, H., Apai, D., Marley, M. S., Saumon, D., Morley, C. V., Buenzli, E., Artigau, É., Radigan, J., Metchev, S., Burgasser, A. J., Mohanty, S., Lowrance, P. J., Showman, A. P., Karalidi, T., Fplateau, D., & Heinze, A. N. 2015, *ApJ*, 798, L13
- Zhang, X. & Showman, A. P. 2014, *ApJ*, 788, L6